Detailed-term-accounting-approximation calculations of the radiative opacity of laser-produced Al plasmas

Jiaolong Zeng, Jianmin Yuan, and Qisheng Lu

Department of Applied Physics, National University of Defense Technology, Changsha 410073, People's Republic of China

An extensive configuration interaction (CI) scheme and the *R*-matrix method are combined to calculate the radiative opacity for laser-produced aluminum plasma in local thermodynamic equilibrium using the detailed-term-accounting (DTA) approximation. The CI scheme is used to obtain the absorption oscillator strengths of the electric dipole allowed transitions for evaluating the bound-bound absorption cross sections, and the *R*-matrix method is used to obtain the bound-free absorption (photoionization) cross sections. For an aluminum plasma at a temperature of 20 eV and the density of 0.01 g/cm^3, the Rosseland and Planck mean opacities are calculated to be 4184 and 24891 cm^2/g, respectively, by integrating the spectrally resolved opacities with Rosseland and Planck weighting functions. The two mean opacities are also obtained by using the average atom model, and they are 22520 and 30402 cm^2/g, respectively. The optical transmission from the photon energy of 70–250 eV, which was experimentally measured by Winhart *et al.* [G. Winhart *et al.* Phys. Rev. E **53**, R1332 (1996)], is also calculated. Generally good agreement is found between our DTA and experimental transmission. Our theoretical result reproduces all structures shown in the experiment, whereas some of the structures near the higher energy edge did not show up in some other opacity models. These structures are attributed to the detailed treatment of the photoionization process.

I. INTRODUCTION

Experimental and theoretical determinations of the radiative opacities of high temperature plasmas have long been of interest. This interest is mainly due to the urgent need for radiative opacities for practical applications, fusion research, and plasma diagnostics. In the past two decades, aluminum plasmas have been of particular concern. Most of these researches on Al plasmas were done in the x-ray region where the spectral range is at $h\nu \gtrsim 1$ keV. Experimentally, many investigations [1–6] were conducted in the x-ray opacities through the measurements of x-ray transmission. All these experiments have been carried out near the energy region of the inner-shell excitations of one $1s$ electron to the $2p$ orbital. Theoretically, a lot of studies [7–11] were carried out to simulate these x-ray transmission spectra. Most of these theoretical studies approximated the *K*-shell-excited states as discrete and only took account of Doppler broadening in calculating the line absorption cross sections. Recently, we [12] (hereafter referred to as paper I) simulated the x-ray transmission through laser-produced Al plasmas using detailed-term-accounting (DTA) approximation. As we have pointed out in paper I, the *K*-shell-excited states are well above the ionization threshold and, therefore, the photoexcitation of a $1s$ electron to the $2p$ orbital should be treated as a photoionization process rather than discrete bound-bound line absorption. All photoabsorption cross sections were obtained by using the close-coupling scheme implemented by *R*-matrix method [13]. We also concluded that the autoionization resonance widths exceed the Doppler widths for most *K*-shell transitions from the low-lying states of Al ions in the plasma. Therefore, the former type of broadening will have a large effect on the radiative opacity and transmission. This effect has been demonstrated clearly in paper I. Since we

included the major broadening mechanism and treated the line absorption and photoionization in a consistent way, our results converged faster and agreed better with experiments than did other detailed calculations.

Compared with the spectral range $h\nu \gtrsim 1$ keV, researches on Al plasmas covering the range $h\nu \lesssim 1$ keV were much fewer. On the other hand, it is this spectral range that determines the Rosseland and Planck mean opacities under typical plasma conditions (most experiments were carried out at temperatures of a few tens of eV). To our knowledge, only a few experimental studies [14,15] were carried out in this spectral range for Al plasmas, although there were indeed some studies with iron plasmas [16–18]. Winhart and co-workers [14,15] measured the spectrally resolved opacities (through transmission) of aluminum in the energy range of 70–280 eV at a typical temperature and density of about 20 eV and 0.01 g/cm^3, respectively. Local thermodynamic equilibrium (LTE) was obtained in their experiment. They also compared the experimental data with some theoretical opacity models [8,19–22].

The purpose of the present work is to calculate the spectrally resolved radiative opacities of the Al plasma in the range $h\nu \lesssim 1$ keV under the experimental condition of Winhart and coworkers [14,15] using the same DTA approximation as in paper I. It can be considered an extension of our previous work presented in paper I, which dealt with the spectral range $h\nu \gtrsim 1$ keV. The Rosseland and Planck mean opacities are then obtained by integrating the spectrally resolved opacities with Rosseland and Planck weighting functions. The calculations have considered bound-bound, bound-free (photoionization), and free-free absorptions and scattering. The required energy levels and absorption oscillator strengths for line absorption cross sections are obtained by the multiconfiguration Hartree-Fock (MCHF) atomic-

structure package [23]. The photoionization cross sections are obtained by using the close-coupling scheme implemented by R-matrix method [13]. In this way, the autoionization resonances and couplings between the channels can be taken into account and the autoionization resonance widths are naturally included in the calculations. As we will demonstrate later, the autoionization resonances at higher photon energies (such as larger than 190 eV) is important to interpret the transmission spectrum. A better agreement with the experiment can be obtained with the inclusion of them than those calculations without them. The free-free absorption and scattering are obtained by using Kramers and Thomson cross sections, respectively.

II. METHOD OF CALCULATION

The method of calculation has been partly introduced in paper I, but it is incomplete for the present calculations. In order to have a complete understanding, we will give a thorough description in the following. This section consists of three parts: (A) populations, (B) radiative opacity, and (C) transmission.

A. Populations

For an LTE plasma of particle density N and temperature T, the population distributions of different ionization stages are given by Saha equation [12,25]

$$\frac{N_{i+1}N_e}{N_i} = \frac{Z_e Z_{i+1}}{Z_i}\exp[-(\phi_i - \Delta\phi_i)/kT], \qquad (1)$$

where N_i is the total population density of ion i, N_e is the number of free electrons per unit volume, ϕ_i is the ionization potential of ion i, $\Delta\phi_i$ is the depression of ionization limit caused by plasma environment restricting the number of bound states available, Z_i and Z_e are the partition functions for ion i and free electron, respectively. They are given by

$$Z_i = \sum_t g_{it}e^{-E_{it}/kT}, \qquad (2)$$

$$Z_e = 2\left(\frac{2\pi m_e kT}{h^2}\right)^{3/2}, \qquad (3)$$

where $g_{it} = (2L_{it}+1)(2S_{it}+1)$ is the statistical weight for term t of ion i in LS coupling condition, L_{it} and S_{it} are the total orbital angular momentum and spin quantum numbers, E_{it} is the energy of term t of ion i above the ground state, k is the Boltzmann constant, T is the temperature, m_e is the electron mass, and h is the Planck constant. The upper limit to the sum (2) is given by the same ionization depression as for the Saha equation. The population density N_{it} for term t of ion stage i is given by the Boltzmann distribution function

$$N_{it} = g_{it}(N_i/Z_i)e^{-E_{it}/kT}. \qquad (4)$$

Equation (1) is solved with the constraint of particle conservation

TABLE I. Calculated IPDs (in eV) and partition functions of different ionization stages of Al ions under the plasma condition of 20 eV temperature and 0.01 g/cm^3 density.

Ions	IPD	Z_i
Al I	1.324	30.8
Al II	2.649	67.8
Al III	3.973	41.1
Al IV	5.298	5.33
Al V	6.622	8.94
Al VI	7.947	15.5
Al VII	9.271	17.4
Al VIII	10.596	20.67

$$N = \sum_{it} N_{it} \qquad (5)$$

and charge conservation

$$N_e = \sum_{it} q_i N_{it}, \qquad (6)$$

where N is the specified total particle density and q_i is the charge of ion i.

In solving the Saha equation (1), a calculation of the ionization potential depression (IPD) is needed to give a finite limit to the partition functions. As we did in paper I, we chose the Debye-Huckel model [24] to calculate the IPD. For the Debye-Huckel model, the IPD is given by

$$\Delta\phi_i = \frac{ze^2}{4\pi\epsilon_0}\sqrt{\frac{e^2 N_e}{\epsilon_0 kT}}, \qquad (7)$$

where z is the charge of the species of interest ($z=1$ for neutral). The calculated IPDs for different relevant ionization stages under the experimental conditions of Winhart and co-workers [14,15] are listed in Table I. The maximum principal quantum number is approximately equal to 7. In the calculations of the energy levels required for the partition functions, the orbitals included in the present calculation and the method of choosing the configurations are the same as those in paper I. The partition functions for ions of different ionization stages calculated according to this prescription are also given in Table I. The calculated partition functions and IPDs are used to solve Saha equation (1) and the final calculated population fractions for various charge states are shown in Fig. 1. One can see from Fig. 1 that the Al V ion is the most abundant, accounting for 50% of the total, next is Al VI ion, accounting for 32%. The average ionization degree is 4.2, which is in excellent agreement with that of OPAL [19] (which equals to 4.3).

B. Radiative opacity

The total absorption coefficient for a plasma of particle density N and temperature T is constructed as the sum of the bound-bound, bound-free, free-free, and scattering combinations. The contribution of bound-bound absorption is made
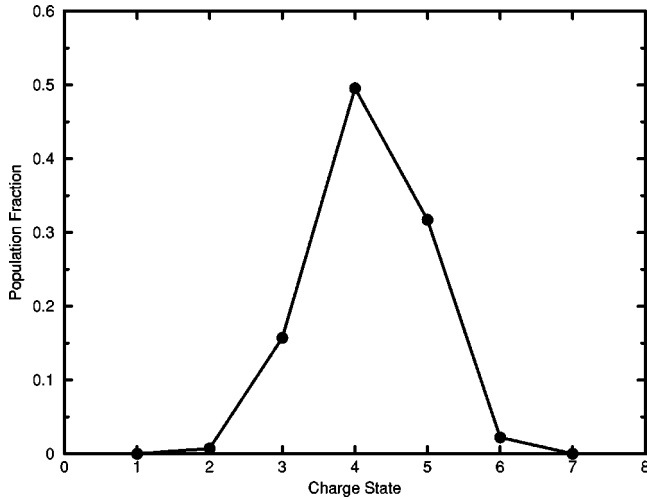
FIG. 1. Population fraction versus the charge state for Al plasma at a temperature of 20 eV and a density of 0.01 g/cm^3.

up of the transitions whose lower and upper states belong to the true bound states, i.e., their energies relative to the ground state are less than the depressed ionization potential. The bound-bound absorption coefficient for radiation of energy $h\nu$ can be obtained from the cross sections of the bound-bound lines

$$\mu_{bb}(h\nu) = \sum_i \left[\sum_{tt'} N_{it}\sigma_{itt'}(h\nu) \right], \qquad (8)$$

where $\sigma_{itt'}(h\nu)$ is the cross section for photoexcitation from term t to t' and can be expressed in terms of the absorption oscillator strength $f_{itt'}$ as

$$\sigma_{itt'}(h\nu) = \frac{\pi h e^2}{m_e c} f_{itt'} S(h\nu) = 109.71 f_{itt'} S(h\nu), \qquad (9)$$

where S is the line shape function with $h\nu$ in eV and $\sigma_{itt'}$ in Mb. If only the Stark broadening is considered, the line shape function has a Lorentzian profile. If only Doppler broadening is considered, the line shape function has a Gaussian profile. In general, the observed spectral profile is neither simply Gaussian nor Lorentzian, but a convolution of these two profiles, i.e., the Voigt profile

$$S(h\nu) = \frac{\sqrt{\ln 2}}{\sqrt{\pi}\Gamma_d} H(a,v), \qquad (10)$$

where $H(a,v)$ is the Voigt function

$$H(a,v) = \frac{a}{\pi} \int_{-\infty}^{+\infty} \frac{e^{-x^2}}{a^2 + (v-x)^2} dx,$$

$$a = \sqrt{\ln 2}\,\Gamma_l/\Gamma_d,$$

$$v = \sqrt{\ln 2}(h\nu - h\nu_0)/\Gamma_d,$$

where Γ_d and Γ_l are the Doppler and Stark half-width at half maximum (HWHM), respectively. The Doppler HWHM is related to the temperature T of the plasma and transition energy $h\nu_0$ [25]

$$\Gamma_d = 3.858 \times 10^{-5}(kT/A)^{1/2}(h\nu_0), \qquad (11)$$

where A is atomic weight of the ion in gram and the units of kT, $h\nu_0$ and Γ are eV. The Stark HWHM (in eV) can be obtained by semiempirical method [26,27]

$$\Gamma_l = N_e \frac{8\pi}{6} \frac{\hbar^3}{m^2 e} \left(\frac{2m}{\pi kT}\right)^{1/2} \frac{\pi}{\sqrt{3}} \left(0.9 - \frac{1.1}{z}\right)$$

$$\times \sum_{j=i,f} \left(\frac{3n_j}{2z}\right)^2 (n_j^2 - l_j^2 - l_j - 1), \qquad (12)$$

where n_i (l_i) and n_f (l_f) are the effective principal (the orbital angular momentum) quantum numbers of the lower and upper energy levels of the transition, respectively.

The contribution of bound-free absorption can be obtained from the photoionization cross sections per ion

$$\mu_{bf}(h\nu) = \sum_i N_i\sigma_i(h\nu), \qquad (13)$$

where $\sigma_i(h\nu)$ is the photoionization cross section per ion i and it can be calculated from the photoionization cross sections $\sigma_{it}(h\nu)$ from term t in ion i

$$\sigma_i(h\nu) = \sum_t \frac{g_{it}e^{-E_{it}/kT}}{Z_i}\sigma_{it}(h\nu). \qquad (14)$$

For the present work, all the photoionization cross sections are obtained using the close-coupling R-matrix method [13]. As the R-matrix method can account for correlation effects between the free and bound electrons and the couplings between different ionization channels, it can give accurate photoionization cross sections, as demonstrated in our previous work [28,29].

The bound-bound and bound-free contributions to the opacity are generally dominant and so only simple approximations are used to describe the free-free and scattering contribution to the opacity. The free-free absorption coefficient is given by

$$\mu_{ff}(h\nu) = \sum_i N_i\sigma_{ff}(h\nu), \qquad (15)$$

where $\sigma_{ff}(h\nu)$ is the Kramers cross section

$$\sigma_{ff}(h\nu) = \frac{16\pi^2 e^2 h^2}{3\sqrt{3}c(2\pi m)^{3/2}} \frac{z^3 N_i g_{ff}}{(kT)^{1/2}(h\nu)^3}, \qquad (16)$$

where z is the ionic charge, the free-free Gaunt factor g_{ff}, is taken as unity. The scattering contribution to the absorption coefficient μ_{scatt} is approximated using Thomson scattering cross section.

The total opacity is related to the absorption coefficient by

$$\rho\kappa'(h\nu) = [\mu_{bb}(h\nu) + \mu_{bf}(h\nu) + \mu_{ff}(h\nu)](1 - e^{-h\nu/kT})$$
$$+ \mu_{scatt}(h\nu). \tag{17}$$

The prime on the opacity denotes that the stimulated emission has been included in the calculation.

In practical applications, such as energy transfer through hot dense matter, Rosseland and Planck mean opacities are required. These two mean opacities are defined by

$$\frac{1}{K_R} = \int_0^\infty \frac{W_R(u)du}{\kappa'(u)} \tag{18}$$

and

$$K_P = \int_0^\infty [\kappa'(u) - \kappa_{scatt}(u)]W_P(u)du, \tag{19}$$

where $u = h\nu/kT$, $\kappa_{scatt}(u)$ is the opacity contributed by scattering, W_R and W_P are Rosseland and Planck weighting functions, respectively, given by

$$W_R(u) = \frac{15}{4\pi^4} \frac{u^4 e^{-u}}{[1 - e^{-u}]^2}$$

and

$$W_P(u) = \frac{15}{\pi^4} \frac{u^3 e^{-u}}{1 - e^{-u}}.$$

C. Transmission

The fraction of radiation transmitted F at energy $h\nu$ with respect to some incident source of arbitrary intensity is given by

$$F(h\nu) = e^{-\rho\kappa'(h\nu)L}, \tag{20}$$

where L is the path length traversed by the light source through the plasma. The function F is integrated over a Gaussian function, with the full width corresponding to the spectrometer resolution, to obtain the final transmission spectrum.

III. RESULTS AND DISCUSSION

Using the method discussed above, we have calculated the radiative opacity under the experimental condition of Winhart and coworkers [14,15] with the temperature of 20 eV and density of 0.01 g/cm³. In their experiment, the aluminum sample layer was 107.5 nm ($\rho L = 30$ μg/cm²) and thus the path length L was determined to be 0.003 cm. The time resolution was 20 ps and the wavelength resolution 0.1 nm.

Figure 2 shows the opacity contributed by bound-bound absorption. It can easily be seen that the bound-bound absorption consists of two main distinct structures. The 0–70 eV energy range consists of $2s$-$2p$ transitions and 70–215 eV energy range the $2p$-ns, and $2p$-nd transitions. For ex-
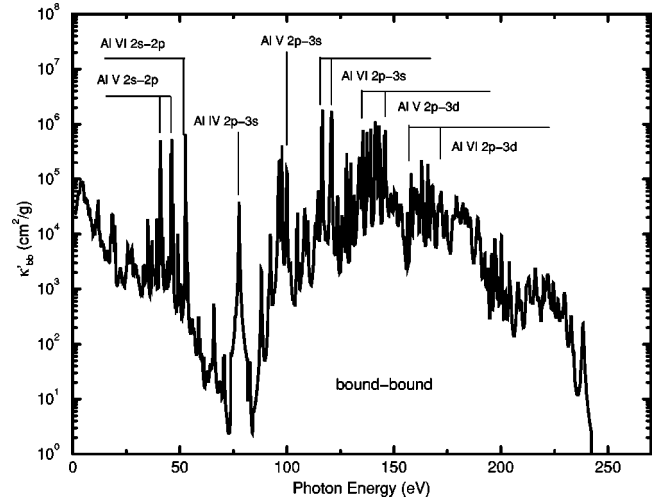

FIG. 2. Radiative opacity contributed by bound-bound absorption for Al plasma at a temperature of 20 eV and a density of 0.01 g/cm³.

amples, the three strongest lines located at 41, 46, and 52 eV are attributed to the $2s$-$2p$ bound-bound transitions from Al V and Al VI ions. The prominent line absorptions near 77, 97, and 116 eV are from the $2p$-$3s$ transitions contributed by Al IV, Al V, and Al VI ions, respectively. As we will demonstrate later, these $2p$-$3s$ absorption lines constitute the most striking structures in the experimental transmission spectrum. The absorptions near 140 and 165 eV are caused by the $2p$-$3d$ transitions of Al V and Al VI ions. Above 240 eV, there are no true bound-bound transitions. The widths of the lines are large enough to fill the gaps between the discrete spectral lines. In the photon energy range shown in the plot, the Stark width is much more larger than the Doppler width, thus the Stark broadening is the major broadening mechanism. As we have demonstrated in a recent paper [30], the Planck mean opacities are nearly equal with and without considering the Stark width, but the Rosseland mean opacities differ considerably depending on whether or not the Stark broadening is taken into account. The Rosseland mean opacities are sensitive to the detailed profile and corresponding width.

Figure 3 shows the opacity contributed by the bound-free absorption, with Fig. 3(a) referring to the result of only taking account of autoionization resonance width and Fig. 3(b) to the result of including both the autoionization resonance width and the Stark width. The opacity shown in Fig. 3(a) is obtained directly from our R-matrix photoionization cross sections. The details of performing the R-matrix calculation can be found in paper I. In order to obtain this result, we include the numbers of the photoionization cross sections of 93, 168, 157, and 146 terms belonging to Al IV, Al V, Al VI, and Al VII ions, respectively. From the inspection of Fig. 3(a), one can see that the autoionization resonance width is not large enough to fill the gaps between the resonances. In fact, under the experimental condition considered, the Stark full width is the largest among all the broadening mechanisms and, therefore, becomes the major factor to be considered. In order to take account of the Stark broadening, we convolute the curve shown in Fig. 3(a) with a Lorentzian
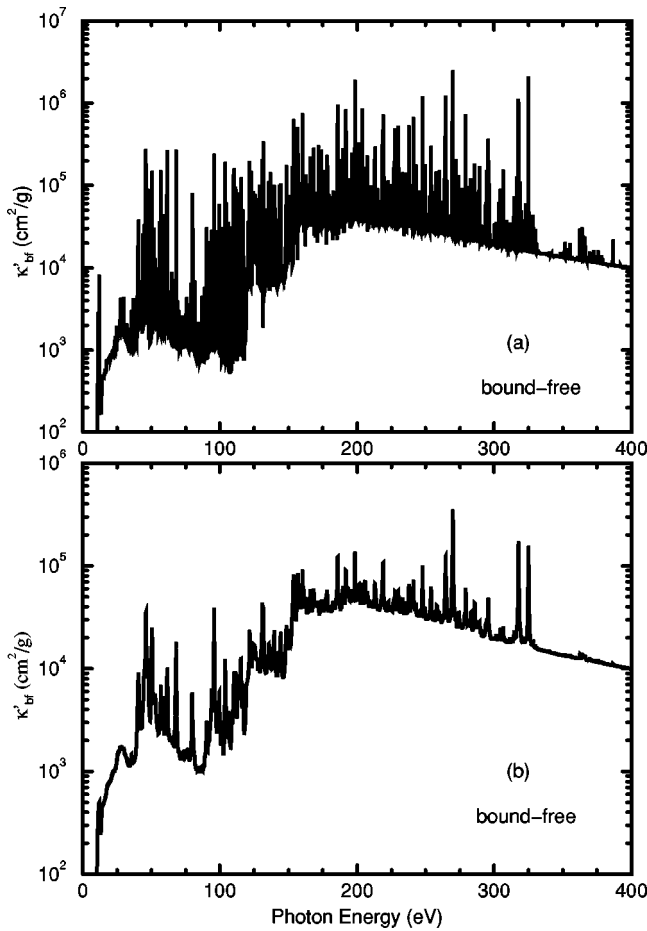
FIG. 3. Radiative opacity contributed by bound-free absorption for Al plasma at a temperature of 20 eV and a density of 0.01 g/cm^3: (a) with only the autoionization resonance width being taken account and (b) with both the autoionization resonance width and Stark width (0.4 eV) being considered.

FIG. 4. Total radiative opacity for Al plasma at a temperature of 20 eV and a density of 0.01 g/cm^3: the solid line refers to the DTA calculation and the dashed line to the AA model. For DTA model, $K_R = 4184$ cm^2/g, $K_P = 24\,891$ cm^2/g; For AA model, $K_R = 22\,520$ cm^2/g, $K_P = 30\,402$ cm^2/g.

profile function, with the full width corresponding to the Stark width. From the estimation of the Stark full width, we take it to be 0.4 eV. The final result, after the Stark broadening has been included, is shown in Fig. 3(b). In this case, the resonance structures coalesce to fill the gaps between them. Many resonance structures are greatly smoothed and some smaller ones can no longer be seen after the convolution. The values of the resonances in the opacity spectrum have also been greatly reduced. The maximum opacity in Fig. 3(a) is more than 2×10^6 cm^2/g, whereas in Fig. 3(b) it is less than 4×10^5 cm^2/g. These results show that the autoionization widths of the valence-shell excited states are in generally by far smaller than the Stark widths.

Figure 4 shows a solid line representing the total opacity with the bound-free absorption shown in Fig. 3(b). One can see that below 200 eV, the major absorption structures in the total opacity are caused by bound-bound transitions; above 200 eV, the opacity consists of a smooth background and many structures caused by the autoionization resonances. It seems that some of these autoionization resonances were not fully included in the opacity models [8,19–22] mentioned above. This can be illustrated later by comparing the theo-
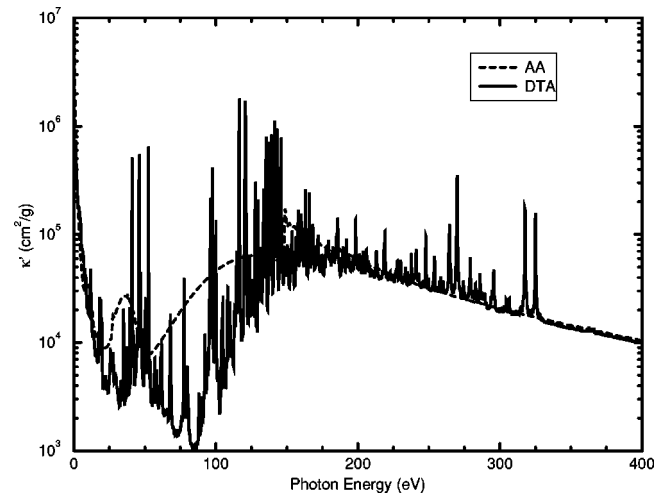
retical transmission obtained by OPAL [19] with the experimental one. The Rosseland and Planck mean opacities obtained according to Eqs. (18) and (19) are 4184 and 24891 cm^2/g, respectively. In order to have a comparison with the opacity obtained by the average atom (AA) model, we have also carried out calculations using the AA model. The result is shown in Fig. 4 with a dashed line. One can see that all the structures are smoothed into a few broad peaks in the AA model. Above 200 eV, the opacities of the AA models are nearly equal to the smooth background of the DTA model. Below 220 eV, however, large difference exists between the two models. The opacity obtained by the AA model is considerably larger than that obtained by the DTA model for photon energy from 20 eV to 120 eV. This difference will, of course, cause large difference between the two models for the Rosseland and Planck mean opacities not only because the opacities obtained from the two models differ considerably, but also because the maxima of the Rosseland and Planck weighting functions are located in this photon energy range. (The Rosseland and Planck weighting functions reach their maxima at approximate 77.6 and 56.8 eV, respectively, at the temperature of 20 eV.) The Rosseland and Planck mean opacities are 22520 and 30402 cm^2/g, respectively, for the AA model. The Rosseland mean opacity by the AA model is more than four times larger than that by the DTA model. The Planck mean opacity, on the other hand, does not have such a large difference between the two models. The value obtained by the AA model is larger than that obtained by the DTA model by only 22%.

In order to testify the correctness and accuracy of our calculations, we have derived the transmission from the calculated opacity shown in Fig. 4 to compare with the experimental spectrum. Figure 5(a) shows the transmission calculated with Eq. (20) in the energy range from 70–250 eV, which corresponds to the range measured by the experiments [14,15]. In this plot, the instrumental broadening has not been included. To compare directly with the experiment, in-
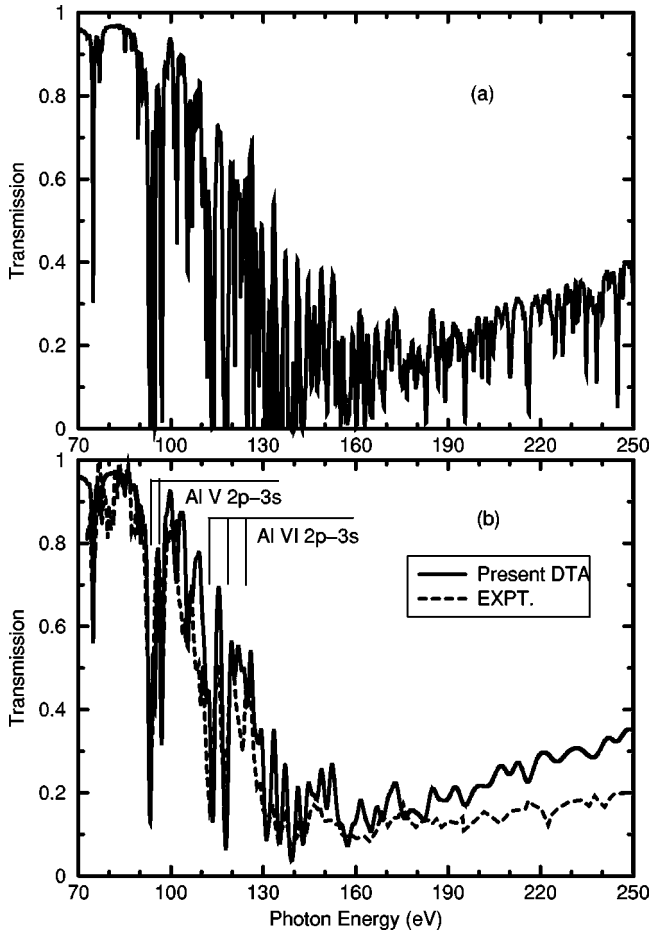
FIG. 5. Transmission calculated as a function of photon energy in eV using DTA approximation: (a) the instrumental broadening having not been considered and (b) integrating curve (a) using the reported spectrometer resolution (solid line). Note that the spectrometer resolution are varied with photon energies. The dashed line is the experimentally observed spectrum [14].

TABLE II. Some calculated weighted oscillator strengths for transitions from the ground state of Al V ion, the length and velocity forms are given to show the quality of our calculation.

Transition	gf_l	gf_v
$(1s^2 2s^2)2p^5 \, ^2P^o$-$2p^4(^1D)3s \, ^2D$	0.4215	0.4189
$2p^5 \, ^2P^o$-$2p^4(^1D)3d \, ^2D$	1.7325	1.7038
$2p^5 \, ^2P^o$-$2p^4(^3P)3d \, ^2D$	0.2449	0.2369
$2p^5 \, ^2P^o$-$2p^4(^1S)3d \, ^2D$	0.4232	0.4140
$2p^5 \, ^2P^o$-$2p^4(^3P)3s \, ^2P$	0.7084	0.7128
$2p^5 \, ^2P^o$-$2p^4(^1D)3d \, ^2P$	1.7031	1.6436
$2p^5 \, ^2P^o$-$2p^4(^3P)3d \, ^2P$	0.5064	0.4892

culated oscillator strengths for the $2p$-$3s$ and $2p$-$3d$ transitions from the ground state of Al V ion. The length and velocity forms are given to show the quality of our calculations. The agreement between the length and velocity forms is rather good, the relative differences being less than 3.5%. From Table II one can see that the oscillator strengths of the $2p$-$3d$ lines are indeed larger than those of the $2p$-$3s$ lines. At higher photon energies (above 160 eV), however, many structures shown in Fig. 5(a) are greatly smoothed after taking account of the instrumental effects. The big differences shown in Figs. 5(a) and 5(b) (the solid line) are, undoubtedly, caused by the instrumental broadening. As reported in the experiment [14,15], the wavelength resolution was 0.1 nm. According to this wavelength resolution, the energy resolution varies considerably in the energy range from 70 to 250 eV, since the energy resolution is in proportion to the square of the photon energy. For example, the energy resolution is 0.82 eV at 100 eV, while it is increased to 1.84, 3.2, and 5.1 eV at 150, 200, and 250 eV, respectively. Because of the low energy resolution at the higher photon energies in the experiment, the structures are smoothed more greatly near the higher energy edge.

One of the most accurate opacity model among those mentioned above is the OPAL [19]. It obtained better agreement with the experiment [14,15] than did other models [8,20–22], therefore, we only compare our DTA transmission spectrum with that of the OPAL [19]. The result is shown in Fig. 6(a), where the solid line refers to our DTA transmission, the long dashed line to the transmission obtained by the OPAL, and the dashed line to the experimental spectrum. One can see that at lower photon energies (less than about 150 eV), both theoretical calculations exhibit similar structures to the experiment. The similarity between the two theoretical results are understandable, because both of the two theories used the atomic structure codes to calculate the relevant atomic parameters, such as, transition energies and dipole oscillator strengths for obtaining the bound-bound absorption cross sections. As has been said above, our DTA model have used the MCHF atomic-structure package [23] to obtain the relevant atomic parameters. The OPAL model has chosen to use prefitted analytic effective potentials as input to the Dirac equation to obtain configurationally averaged energies. Then the configurational averages were split into term energies by using standard perturbation methods in either LS or intermediate coupling. In addition, at these lower photon energies,
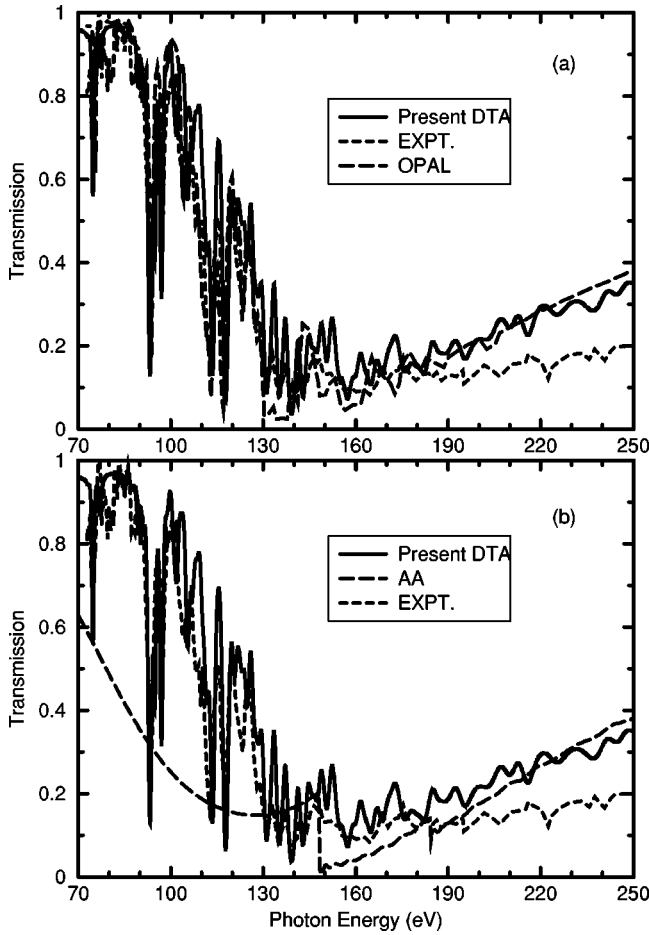
strumental effects must be included. Figure 5(b) shows a solid line obtained by convoluting the curve shown in Fig. 5(a) with the spectrometer resolution, which varies with the photon energy. The dashed line in Fig. 5(b) refers to the experimental spectrum. In order to have an optimum coincidence with the experimental spectrum, our DTA result has been shifted to lower photon energies by 2.6 eV. From the comparisons of the Figs. 5(a) and 5(b), one can easily see that the spectrum shown in Fig. 5(a) is more highly resolved than that in Fig. 5(b). The detailed features shown in Fig. 5(a) should be observable in high-resolution measurements. Generally good agreement is found between our DTA result and the experiment. In Figs. 5(a) and 5(b), the most striking structures near 75, 95, and 114 eV are caused by the $2p$-$3s$ bound-bound transitions of Al IV, Al V, and Al VI ions, respectively. The structures around 140 eV and 165 eV are caused by the $2p$-$3d$ transitions of Al V and Al VI ions, respectively. The structures caused by $2p$-$3d$ transitions are made less striking by the stronger bound-free background absorption. As a matter of fact, the $2p$-$3d$ lines are more stronger than those of $2p$-$3s$ ones. Table II gives some cal-

FIG. 6. Comparisons between our DTA simulation and other theoretical models: (a) OPAL [19] and (b) AA.

TABLE III. Some calculated excitation energies ΔE (eV) and oscillator strengths for some ^3P-$^3D^o$ transitions whose excitation energies are larger than 210 eV from the ground state of Al VI ion. For oscillator strengths, the length f_l and velocity f_v forms are given.

Transition	ΔE (eV)	f_l	f_v
$2s^2 2p^4\,^3P$-$2s(^2S)2p^4(^3P)(^2P)4p\,^3D^o$	212.172	0.098	0.102
$2s^2 2p^4\,^3P$-$2p^5(^2P^o)3d\,^3D^o$	224.321	0.023	0.025
$2s^2 2p^4\,^3P$-$2s(^2S)2p^4(^3P)(^2P)5p\,^3D^o$	226.167	0.032	0.030
$2s^2 2p^4\,^3P$-$2s(^2S)2p^4(^3P)(^2P)6p\,^3D^o$	233.305	0.015	0.017

the autoionization resonances do not have large effects on the opacity or transmission. This is because the opacities caused by the autoionization resonances are by far smaller than those caused by bound-bound absorption. This conclusion can easily be seen from the comparison of the opacities contributed by the bound-bound and bound-free absorptions, which are shown in Figs. 2 and 3(b). The maximal opacity caused by bound-bound absorption is more than 10^6 cm^2/g, while that by bound free is about 4×10^4 cm^2/g. Moreover, the background of the bound-free absorption is relatively large because this photon energy range is very close to the ionization threshold. All these features are different from the situation presented in paper I. Paper I dealt with the photon energy range 1480–1610 eV, which is far above the ionization threshold. Therefore, the background of the bound-free absorption is very weak compared with the absorption caused by the inner-shell transitions of one $1s$ electron being excited into the $2p$ orbital. Furthermore, there is no true bound-bound absorption in the range 1480–1610 eV. As a result, the autoionization resonances at the lower photon energies do not have such large effects on the opacity or transmission as in paper I.

At the higher photon energies, however, our DTA transmission exhibits more structures than that of the OPAL [19]. OPAL [19] did not reproduce some structures at the higher

photon energies, while these structures are indeed verified in the experiment [14,15]. We attribute the structures at the higher photon energies to the more detailed treatment of the photoionization process in our calculations. As indicated above, all the photoionization cross sections required are obtained by close-coupling R-matrix method [13] that is very effective to take account of the autoionization resonances. On the other hand, OPAL [19] obtained their photoionization cross sections using parametric potential approach, which was described by the authors as in Ref. [31]: the parametric potential approach produces photoionization cross sections comparable in accuracy to single configuration, self-consistent-field calculations. The different treatment of the photoionization process may be the reason that whether there are structures or not above 210 eV. On the other hand, both the two models deviate from the experimental spectrum at higher photon energies. The deviation becomes larger and larger as the photon energy becomes higher and higher until 250 eV. The deviation of the both models from the experiment may be caused by the noise, but, in general, the noise can not cause the structures. In order to demonstrate the existence of the structures at the higher photon energy range, we have traced out their origins. As has been pointed out above, under the plasma condition of 20 eV temperature and 0.01 g/cm^3 density, Al V ions account for 50% and Al VI 32%. Take Al VI as an example. Table III gives the calculated excitation energies and oscillator strengths of some ^3P-$^3D^o$ transitions whose excitation energies are larger than 210 eV from the ground state of Al VI ion. These dipole transitions correspond to some structures at the higher photon energies. In addition to the transitions listed in Table III, there are many other such transitions from the excited states of Al VI. Moreover, Al V ions also contribute a lot to such transitions. Due to the poorer resolution power at the higher photon energies, these structures are merged together into a few observable ones. From these analyses, we maintain that the structures observed by the experiment [14,15] at the higher photon energies should be real, not just noise.

The transmission obtained by the AA model is also compared with our DTA and the experimental spectra, which is shown in Fig. 6(b). At lower energies, the transmission obtained by the AA model differs greatly from that of the DTA and of the experiment. Above 200 eV, on the other hand, the transmission obtained by the AA model is very similar to that of the OPAL model shown in Fig. 6(a) and both of them do not reproduce the resonance structures above the threshold.

In Fig. 4, we have seen that above 200 eV the AA model generates the structureless bound-free opacities that are nearly equal to the background of the present DTA model. Therefore, the differences between the present DTA and AA models above 200 eV shown in Fig. 6(b) are mainly caused by the autoionization resonance structures taken into account by the present DTA model. This also gives an indirect support to our conclusion that the differences between the present DTA model and the OPAL model above 200 eV are mainly attributed to the autoionization resonances.

In the present model, the density effects were taken into account very simply by just excluding the electron states above $n=7$, while free atomic wave functions are used in the calculations of all the atomic energy levels and atomic processes cross sections. In a more reasonable treatment of the density effects, the influences of the environment on the atomic wave functions should be considered. As an example, due to the environment effects some of the electron states become shape resonance ones [32], which are quasistationary states in the continimum and are formed by the combining potential barrier of the attractive atomic potential and the centrifugal repulsion of $l(l+1)/r^2$. The R-matrix method can be used to treat this kind of states very effectively [33]. The basic idea of the R-matrix method is to divide the configuration space into two regions. In the inner region, $0 \leqslant r \leqslant r_0$, the correlation effect is treated by the conventional configuration interaction scheme, while in the outer region, $r_0 \leqslant r \leqslant \infty$, a close-coupling equation is solved. The final solution is obtained by matching the wave function at the R-matrix boundary r_0. If the influences of the environment on the atomic wave functions inside and outside the R-matrix boundary have been considered reasonably, the R-matrix method can be used effectively to generate the atomic processes cross sections in the plasmas where the density has considerable effects. Nevertheless, the treatment to the influences of the environment on the atomic wave functions is still far from complete.

In summary, we have calculated the spectrally resolved radiative opacity of Al plasma under a typical experimental condition at a temperature of 20 eV and a density of 0.01 g/cm^3 using the detailed-term-accounting (DTA) approximation. Complex structures, including those caused by bound-bound and bound-free absorptions, dominate the opacity spectrum. The Rosseland and Planck mean opacities obtained by our DTA calculation are determined to be 4184 and 24 891 cm^2/g, respectively. The DTA result differs considerably from that of the AA model for the Rosseland mean opacity (22 520 cm^2/g), although the Planck mean opacity (30 402 cm^2/g) is roughly close to that of the DTA calculation. From the spectrally resolved opacity, we have obtained the transmission. Generally good agreement is found between our DTA transmission and the experimental spectrum. All the structures caused by the $2p$-$3s$ bound-bound lines are reproduced in our DTA calculation. At the higher photon energies, our DTA transmission exhibits more structures, which also showed up in the experiment, than that of the OPAL. We attribute the good agreement with the experiment at the higher energies to the detailed treatment of the photoionization process.

[1] S.J. Davidson, J.M. Foster, C.C. Smith, K.A. Warburton, and S.J. Rose, Appl. Phys. Lett. **52**, 847 (1988).

[2] S. J. Davidson, C.L.S. Lewis, D. O'Neill, S.J. Rose, J.M. Foster, and C.C. Smith, in *Laser Interaction with Matter*, edited by G. Velarde, E. Minguez, and J.M. Perlado (World Scientific, Singpore,1989).

[3] T.S. Perry, S.J. Davidson, F.J.D. Serduke, D.R. Bach, C.C. Smith, J.M. Foster, R.J. Doyas, R.A. Ward, C.A. Iglesias, F.J. Rogers, J. Abdallah, Jr., R.E. Stewart, J.D. Kilkenny, and R.W. Lee, Phys. Rev. Lett. **67**, 3784 (1991).

[4] C.A. Iglesias, M.H. Chen, D.L. McWilliams, J.K. Nash, and F.J. Rogers, J. Quant. Spectrosc. Radiat. Transf. **54**, 185 (1995).

[5] L. Aschke, S. Depierreux, K.G. Estabrook, K.B. Fournier, J. Fuches, S. Glenzer, R.W. Lee, W. Rozmus, R.S. Thoe, and P.E. Young, J. Quant. Spectrosc. Radiat. Transf. **65**, 23 (2000).

[6] C. Chenais-Popovics, F. Gilleron, M. Fajardo, H. Merdji, T. MiBalla, J.C. Gauthier, P. Renaudin, S. Gary, J. Bruneau, F. Perrot, T. Blenski, W. Fölsner, and K. Eidmann, J. Quant. Spectrosc. Radiat. Transf. **65**, 117 (2000).

[7] D.P. Kilcrease, J. Abdallah, Jr., J.J. Keady, and R.E.H. Clark, J. Phys. B **26**, L717 (1993).

[8] S.J. Rose, J. Phys. B **25**, 1667 (1992).

[9] J. Abdallah, Jr. and R.E.H. Clark, J. Appl. Phys. **69**, 23 (1991).

[10] C.A. Iglesias, J.K. Nash, M.H. Chen, and F.J. Rogers, J. Quant. Spectrosc. Radiat. Transf. **51**, 125 (1994).

[11] A. Rickert, J. Quant. Spectrosc. Radiat. Transf. **54**, 325 (1995); S.J. Rose, *ibid.* **51**, 317 (1994).

[12] Jiaolong Zeng, Fengtao Jin, Jianmin Yuan, Qisheng Lu, and Yongsheng Sun, Phys. Rev. E **62**, 7251 (2000).

[13] K.A. Berrington, W.B. Essner, and P.H. Norrington, Comput. Phys. Commun. **92**, 290 (1995).

[14] G. Winhart, K. Eidmann, C.A. Iglesias, A. Bar-Shalom, E. Minguez, A. Rickert, and S.J. Rose, J. Quant. Spectrosc. Radiat. Transf. **54**, 437 (1995).

[15] G. Winhart, K. Eidmann, C.A. Iglesias, and A. Bar-Shalom, Phys. Rev. E **53**, R1332 (1996).

[16] L.B. DaSilva, B.J. MacGowan, D.R. Kania, B.A. Hammel, C.A. Back, E. Hsieh, R. Doyas, C.A. Iglesias, F.J. Rogers, and R.W. Lee, Phys. Rev. Lett. **69**, 438 (1992).

[17] P.T. Springer, D.J. Fields, B.G. Wilson, J.K. Nash, W.H. Goldstein, C.A. Iglesias, F.J. Rogers, J.K. Swenson, M.H. Chen, A. Bar-Shalom, and R.E. Stewart, Phys. Rev. Lett. **69**, 3735 (1992).

[18] P.T. Springer, K.L. Wong, C.A. Iglesias, J.H. Hammer, J.L. Porter, A. Toor, W.H. Goldstein, B.G. Wilson, F.J. Rogers, C. Deeney, D.S. Dearborn, C. Bruns, J. Emig, and R.E. Stewart, J. Quant. Spectrosc. Radiat. Transf. **58**, 927 (1997).

[19] F.J. Rogers and C.A. Iglesias, Astrophys. J., Suppl. Ser. **79**, 507 (1992).

[20] E. Mínguez, J.F. Serrano, and M.L. Gámez, Laser Part. Beams **6**, 265 (1988).

[21] A. Bar-Shalom, J. Oreg, W.H. Goldstein, D. Shvarts, and A. Zigler, Phys. Rev. A **40**, 3183 (1989).

[22] A. Bar-Shalom, J. Oreg, and W.H. Goldstein, J. Quant. Spectrosc. Radiat. Transf. **51**, 27 (1994).

[23] C.F. Fischer, Comput. Phys. Commun. **64**, 369 (1991).

[24] D.J. Heading, J.S. Wark, G.R. Bennett, and R.W. Lee, J. Quant. Spectrosc. Radiat. Transf. **54**, 167 (1995), and references therein.

[25] R. D. Cowan, *Theory of Atomic Spectra* (University of California Press, Berkeley, 1981).

[26] M.S. Dimitrijevic and N. Konjevic, J. Quant. Spectrosc. Radiat. Transf. **24**, 451 (1980).

[27] M.S. Dimitrijevic and N. Konjevic, Astron. Astrophys. **172**, 345 (1987).

[28] Jiaolong Zeng, Jianmin Yuan, Zengxiu Zhao, and Qisheng Lu, Eur. Phys. J. D **11**, 167 (2000).

[29] Jiaolong Zeng, Jianmin Yuan, and Qisheng Lu, Phys. Rev. A **62**, 022713 (2000).

[30] Jiaolong Zeng, Fengtao Jin, and Jianmin Yuan, Chin. Phys. Lett. **18**, 924 (2001).

[31] F.J. Rogers, C.A. Iglesias, and B.G. Wilson, in *Atomic Processes in Plasmas*, edited by Yong-ki Kim and C. E. Raymond, AIP Conf. Proc. No. 206 (AIP, New York, 1990), p. 82.

[32] C.M. Lee and E.I. Thorsos, Phys. Rev. A **17**, 2073 (1978).

[33] Jianmin Yuan and L. Fritsche, Phys. Rev. A **55**, 1020 (1997); Jianmin Yuan, *ibid.* **61**, 012704 (2000).